# Carbon dots decorated ultrathin CdS nanosheets enabling *in-situ* anchored Pt single atoms: A highly efficient solar-driven photocatalyst for hydrogen evolution

Shujun Qiu[a], Yongli Shen[a], Guijuan Wei[a], Shuang Yao[a], Wei Xi[a], Miao Shu[b], Rui Si[b,*], Min Zhang[a], Junfa Zhu[c], Changhua An[a,*]

[a] *Tianjin Key Laboratory of Organic Solar Cells and Photochemical Conversion, School of Chemistry and Chemical Engineering and Tianjin Key Laboratory of Advanced Functional Porous Materials, Institute of New Energy Materials & Low-Carbon Technologies, Tianjin University of Technology, Tianjin 300384, China*
[b] *Shanghai Synchrotron Radiation Facility, Shanghai Institute of Applied Physics, Chinese Academy of Sciences, Shanghai, 201204, China*
[c] *National Synchrotron Radiation Laboratory, University of Science and Technology of China, Hefei, Anhui, 230029, China*

## ARTICLE INFO

## ABSTRACT

Maximizing the usage of cocatalyst to provide fruitful proton reduction sites and suppress charge carrier recombination is an effective stratagy to dramatically improve the photocatalytic performance. Herein, anchoring single atoms (SAs) of Pt onto the ultrathin porous CdS@carbon dots (CDs) nanosheets has been achieved through *in-situ* reduction of Pt precursor. X-ray absorption fine structure spectra identify that the single Pt atoms are bonded as Pt-S with a coordination number 4, due to the scattering between platinum center and the sulfur atoms. The Pt single atoms exhibit strong capacity to trap photo-generated electrons, rendering CdS@CDs/Pt-SAs as a class of efficient solar-driven photocatalyst. It shows an outstanding activity towards $H_2$ generation at rate of 45.5 mmol $h^{-1}$ $g^{-1}$, which is 133 times of that for bare CdS@CDs. The novel method can be extended to the preparation of various functional nanocatalysts owing to its versatility and facileness.

## 1. Introduction

The creation of hydrogen fuel by photocatalytic water splitting with solar energy is an effective strategy to mitigate the increasing energy demand of modern society [1–4]. The hydrogen-energy process chain consists of four major steps: hydrogen production [5,6], hydrogen storage [7,8], regeneration [9] and application as fuel cell etc. The key to enhance hydrogen production efficiency is to get an efficient photocatalyst, usually semiconductor is preferred, which is endowed with the capacity to create electron-hole (e–h) pairs and thus initiated related redox reactions [10–15]. Semiconductor nanoparticles have more reactive surface area, especially low dimensional nanomaterials with dangling bonds. Compared to other dimensional counterparts, ultrathin two-dimensional (2D) photocatalysts have a higher surface/volume ratio. These figures of merits afford them to accelerate e–h separation capability, and fast move charge carriers. However, the high recombination rate of electron–hole pairs is still a main obstacle to inhibit their migration to the surface active sites, resulting low activity even though sacrificial species are introduced into the reaction system. Therefore, integrating an advanced cocatalysts or promoters onto the

surfaces of a proper semiconductor photocatalysts is often a requisite [16–19].

Carbon nanomaterials, including graphene [20,21], carbon nanotubes, and carbon dots (CDs), have been hybridizeded with certain photocatalysts to enhance electron-hole separation, inhibit recombination of the electron-hole pairs and thus boost the performance [22–24]. Among various kinds of promoters, Pt is still the best one. Unfortunately, the scarcity and high cost restrict its further practical applications [25–30]. Therefore, the use of a minimal amount is an urgent mission without compromise the catalytic efficiency. Recently, using atomic-scale metal species can significantly increase the number of catalytic active sites on the surface of the catalyst where basically all the isolated metal atoms are ideally accessible to reactants [31–35]. In this respect, metal atom catalysts possess the following interesting properties: i) atomically dispersed metal centers; ii) coordinatively unsaturated metal active sites; iii) electron confinement/quantum size effects; and iv) strong metal-solid support interactions [36–39]. These features enable them to expose uniform maximum reaction sites, simultaneously boosting both the catalytic activity and selectivity for various reactions. These developments inspire the exploration of single-

atom photocatalytic systems with significantly enhancing their corresponding performance. For example, isolated Pt single atoms (SAs) anchored on g-C$_3$N$_4$ (Pt-CN) with high dispersion and stability can achieve the enhancement of the photocatalytic H$_2$ evolution activity [40]. Yao and coworkers reported a single Ni Atoms on nitrogen-doped graphene not only serve as an electron storage medium to suppress electron-hole recombination, but also as an active catalyst for proton reduction reaction. However, the irregular shaped support catalysts lead to the uncertainty in understanding the process of carrier transfer and associated following redox reactions [41]. Recently, Ye et al realized the decoration of isolated platinum atoms onto the CdS nanowires, in which the maximum utilization of Pt atoms can greatly boost the photocatalytic hydrogen evolution efficiency [42]. Xiong et al reported that the single-atom Co sites coordinated on the partially oxidized graphene nanosheets can be a highly active and durable heterogeneous catalyst for CO$_2$ conversion, wherein the graphene bridges homogeneous light absorbers with single-atom catalytic sites for the efficient transfer of photoexcited electrons [43]. These progresses make great strides on the single-atom candidates towards improving the photocatalytic performance in certain reactions. However, the efficiency is still far from practical requirements, and the development of ease of synthesis and re-productivity strategy to get highly efficient single-atom photocatalytic system still remains elusive.

In this work, we firstly prepared ultrathin CdS@CDs nanosheets through *in-situ* conversion of CDs aided grown Cd(OH)$_2$ nanosheets, accelerating the separation of photo-generated electrons and holes by minimizing the distance through which the electrons have to migrate before reaching the solid/water interfaces. Then single Pt atoms were concurrently produced by carbon dots to achieve ultrathin 2D CdS@CDs/Pt-SAs nanohybrids, representing a new scheme for solar energy conversion for more energy-efficient catalytic hydrogen evolution and related catalytic reactions. The introduction of CDs and Pt SAs increases the solar utilization, charge separation rate, and surface active sites, and thus significantly enhanced the photocatalytic water splitting efficiency. The solar-driven hydrogen evolution over ultrathin 2D CdS@CDs/Pt-SAs nanohybrids is as 133 folds as single CdS@CDs nanosheets. The formation of Pt-S bonds between unsaturated sulfur atoms of CdS with isolated platinum atoms promises the high stability of the newly constructed catalysts. The extended X-ray absorption fine structure (EXAFS) spectroscopy verifies that Pt atoms have been atomically anchored on the surfaces of CdS@CDs with unsaturated coordination geometry. Moreover, photoluminescence (PL) decay tests and density functional theory (DFT) calculations reveal that Pt SAs have the strong capacity to accept photo-generated electrons and maximize the reaction sites, and thus promote directional migration of photogenerated excitons to the platinum atoms, supplying long-lived electrons for the reduction of water splitting into hydrogen.

## 2. Experimental section

### 2.1. Materials

All the chemical materials were used as received without further purification. Cadmium acetate dihydrate (Cd(CH$_3$COO)$_2$·2H$_2$O), n-Butylamine (C$_4$H$_{11}$N), sodium sulfide nonahydrate (Na$_2$S·9H$_2$O) and ethylene glycol (C$_2$H$_6$O$_2$) were obtained from Aladdin. H$_2$PtCl$_6$·6H$_2$O was purchased from Macklin. And sodium sulfite (Na$_2$SO$_3$) was received from Sinopharm Chemical Reagent Co., Ltd. (Shanghai, China). Deionized distilled water was used in all the experiments.

### 2.2. Synthesis of CDs, CdS@CDs, and CdS@CDs/Pt-SAs nanosheets

CDs were prepared by electrochemically anodic oxidation of alcohol in NaOH solution (0.17 mol L$^{-1}$) of 140 mL ethanol and 10 mL water. Two pieces of platinum sheets (1.5 cm × 1.5 cm) were used as anode and counter electrode, respectively. A direct-current power supply with

a static potential of 15 V (current density ˜ 90 mA·cm$^{-2}$) was used. After electrolysis of 24 h, dark brown solution was produced. Then the solution was subjected to spin evaporation treatment. The obtained solid was dissolved in 100 mL of deionized water, and to be dialyzed for 24 h [44].

The Cd(OH)$_2$@CDs nanosheets were firstly synthesized by a solvothermal method. In a typical procedure, 0.1 g of cadmium acetate was dissolved in a mixture of 30 mL of water dispersion of CDs (4 mg· mL$^{-1}$), 20 mL of ethylene glycol and 0.8 mL n-butylamine under stirring. Then the mixture was transferred to a 100 mL Teflon-lined stainless-steel autoclave. The autoclave was sealed and maintained at 120 °C for 5 h. After the reaction was complete, it was cooled to room temperature naturally. The obtained Cd(OH)$_2$@CDs was rinsed with distilled water and ethanol several times, collected by centrifugation, and then dried in a vacuum at 60 °C overnight (For comparison, here we also synthesized Cd(OH)$_2$ nanosheets with 10 mL and 40 mL of carbon dots, respectively. Corresponding SEM images (Fig. S1c and d) revealed that the thick nanosheets and agglomerated sheets were resulted. So the sample synthesized with 30 mL CDs was applied in the following work). Then 150 mL aqueous solution of Na$_2$S (3 mmoL·L$^{-1}$) was added into 60 mL water dispersion of Cd(OH)$_2$@CDs (2 mmoL·L$^{-1}$) and stirred 15 min, subsequently 150 mL Na$_2$S solution (6 mmoL·L$^{-1}$) was added and maintained additional 15 min. The obtained CdS@CDs (23.28 wt%) was treated as above and collected for anchoring single-atoms.

Pt single atoms anchored CdS@CDs (CdS@CDs/Pt-SAs) was synthesized by an *in-situ* reduction of Pt source with loaded CDs without using external reductants. Typically, the as-prepared CdS@CDs (16 mg) nanosheets were dispersed in 8 mL distilled water, then 20 mL aqueous solution of H$_2$PtCl$_6$·6H$_2$O (0.06 mg mL$^{-1}$) was dropwisely introduced with a syringe pump and kept stirring 4 h at room temperature. The final product was filtered and washed with deionized water and absolute ethanol to remove the excess of Pt species and substituted chloride ions on the surfaces of CdS@CDs. Pt nanoparticles decorated CdS@CDs (CdS@CDs/Pt-NPs) was also synthesized by increasing quantity of H$_2$PtCl$_6$·6H$_2$O (0.08 mg mL$^{-1}$).

### 2.3. Characterization

The morphology and microstructure of the as-prepared products were studied by scanning electronic microscope (SEM; ZEISS MERLIN Compact, Germany), transmission electron microscope (TEM; Tecnai G2 Spirit TWIN, FEI), High-Resolution Transmission Electron Microscope (HRTEM) with FEG (Talos F200 X), and the High-Angle Annular Dark Field Scanning Transmission Electron Microscopy (Titan Themis Cubed G2 60–300). X-ray diffraction (XRD) was carried out on a Rigaku Corporation UItimaIV diffractometer with a Cu Kα radiation source (λ = 1.5418 nm) operated at 40 kV and 40 mA. X-ray photoelectron spectroscopy (XPS) measurements were performed on an ESCALAB 250Xi system. The UV–vis diffuse reflectance absorption spectrum was recorded on a Hitachi/U-3900 UV–vis spectrophotometer. The photoluminescence (PL) was obtained from a FL3-2-IHR221-NIR-TCSPC. Time-resolved transient PL decay spectrum was performed on a Micro Time 200 spectrometer. The X-ray absorption fine structure (XAFS) spectrum at Pt L$_3$ (E$_0$ = 11,564.0 eV) edge was performed at BL14W1 beamline of Shanghai Synchrotron Radiation Facility(SSRF) operated at 3.5 GeV under "top-up" mode with a constant current of 250 mA. The elemental composition was tested by Inductively Coupled Plasma Mass Spectrometer (ICP-MS, iCAP RQ, Germany) and Elementar Analysensysteme GmbH (Vario EL Cube, Germany).

### 2.4. Photoelectrochemical measurements

The photoelectrodes were prepared as follows. 5 mg of the as-obtained photocatalyst powder was dispersed into 600 u L of ethanol and 40 u L Nafion under ultrasonication. Then the mixture was coated onto
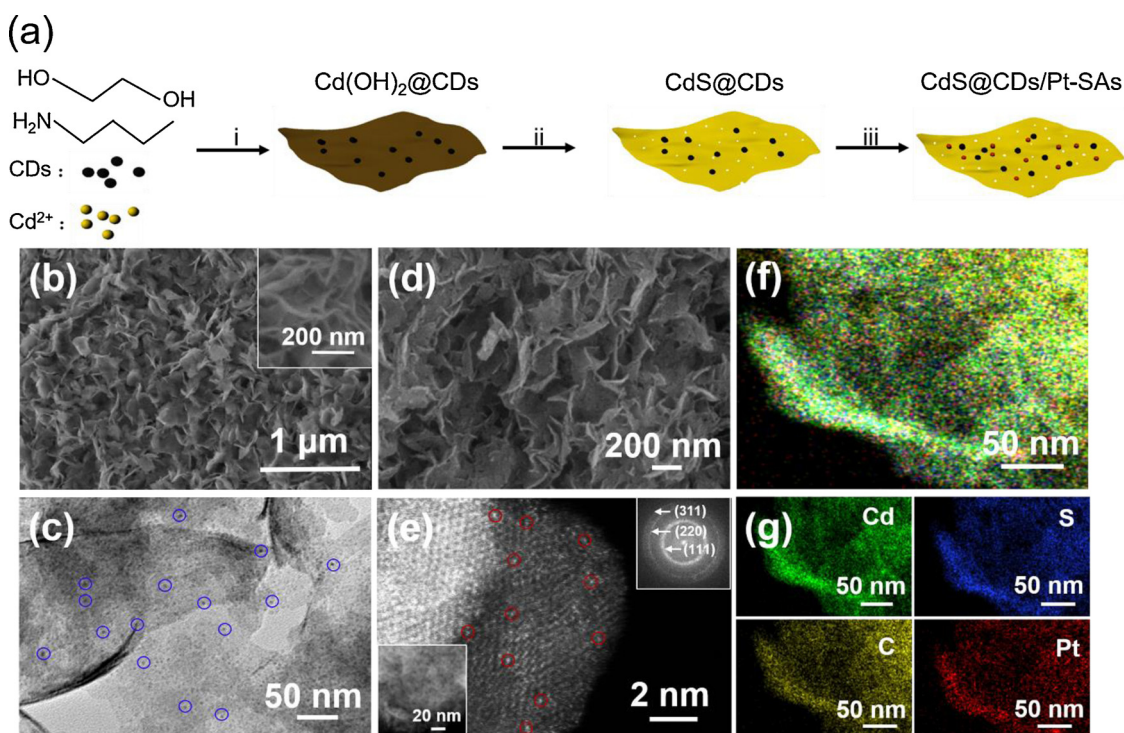
**Fig. 1.** (a) A schematic illustration for the synthesis of CdS@CDs/Pt-SAs: i) Cd(OH)$_2$@CDs was synthesized by the reaction of cadmium acetate with n-butylamine in a mixture of ethylene glycol and CDs aqueous solution by a solvothermal method, ii) Reaction of sulfidation process to produce CdS@CDs, iii) Pt single-atoms were loaded by an *in-situ* impregnation and conversion; (b) SEM image and (c) HRTEM image for Cd(OH)$_2$@CDs, (d) SEM image and (e) HAADF-STEM image of CdS@CDs/Pt-SAs, the insets show the HRTEM image (bottom-left) and SAED pattern (up-right), and (f, g) EDS elemental mapping of CdS@CDs/Pt-SAs.

a 1.0 × 1.0 cm$^2$ FTO glass electrode. The photoelectrochemical system was constructed in a conventional three-electrode system with a Pt electrode and Ag/AgCl electrode as the counter electrode and reference electrode, respectively. The electrochemical impedance spectroscopy (EIS) was tested in a 0.5 M Na$_2$SO$_4$ aqueous solution ranging from 100,000 to 0.01 Hz. The photoelectrochemical tests were carried out on an electrochemical workstation (CHI-760E, Shanghai Chenhua Company, China) in a three-electrode cell with 0.5 M Na$_2$SO$_4$ as electrolyte at room temperature under visible light.

### 2.5. Calculation of quantum yield (QE)

The average intensity of incident-light was determined by a CEL-NP2000 optical power meter (CEAULIGHT). The average rate of hydrogen production was derived from the amount of hydrogen produced at a certain time. The number of incident photons (N) is calculated by Eq. (1).

$$N = \frac{E\lambda}{hc} \qquad (1)$$

In Eq. (1), $E$ is the average intensity of irradiation, $\lambda$ represents wavelength of light, $h$ stands for the Planck constant, and $c$ is the speed of light, respectively.

The QE for H$_2$ production at monochromatic light irradiation was calculated from Eq. (2).

$$QE = \frac{2 \times number\ of\ evolved\ H_2\ molecules}{number\ of\ incident\ photons} \times 100\% \qquad (2)$$

### 2.6. Evaluation of photocatalytic hydrogen evolution

The photocatalytic hydrogen evolution was evaluated on a Labsolar-6A system (PefectLight Company, Beijing China), where a 300 W Xe arc lamp (CEL-HXF300/300UV, CEAUlight Company, Beijing China) was

used as simulated sunlight source. The as-fabricated photocatalyst samples (10 mg) were added into an aqueous solution containing 0.35 M Na$_2$SO$_3$ and 0.25 M Na$_2$S (60 mL) in a quartz vial. The evolved H$_2$ was detected using an online gas chromatography (GC7900, Techcomp) equipped with a 0.5 nm molecular sieve column.

### 2.7. X-ray absorption fine structure (XAFS) measurements

The X-ray absorption fine structure spectra at Pt L$_3$ ($E_0$ = 11,564.0 eV) edge was performed at BL14W1 beamline of Shanghai Synchrotron Radiation Facility (SSRF) operated at 3.5 GeV under "top-up" mode with a constant current of 250 mA. The XAFS data were recorded under fluorescence mode with a Lytle ion chamber. The energy was calibrated accordingly to the absorption edge of pure Pt foil. Athena and Artemis codes were used to extract the data and fit the profiles. For the X-ray absorption near edge structure (XANES) part, the experimental absorption coefficients as function of energies $\mu(E)$ were processed by background subtraction and normalization procedures, and reported as "normalized absorption" with $E_0$ = 11,564.0 eV for the measured sample and PtO$_2$/Pt foil standard. Based on the normalized XANES profiles, the molar fraction of Pt$^{4+}$/Pt$^0$ can be determined by the linear combination fit [45] with the help of various references (Pt foil for Pt$^0$ and PtO$_2$ for Pt$^{4+}$). For the extended X-ray absorption fine structure (EXAFS) part, the Fourier transformed (FT) data in $R$ space were analyzed by applying first-shell approximate model for Pt-S contribution. The passive electron factors, $S_0^2$, were determined by fitting the experimental data on Pt foil and fixing the coordination number (CN) of Pt-Pt to be 12, and then fixed for further analysis of the tested samples. The parameters describing the electronic properties (e.g., correction to the photoelectron energy origin, $E_0$) and local structure environment including CN, bond distance ($R$) and Debye-Waller factor around the absorbing atoms were allowed to vary during the fit process. The fitted ranges for $k$ and $R$ spaces were selected to be $k$ = 3–12 Å$^{-1}$ with $R$ = 1.3–2.5 Å ($k^3$ weighted).

## 2.8. Theoretical calculations

All the calculations presented in this work were performed using the generalized gradient approximation (GGA)-Perdew, Burke and Ernzerhof (PBE) as implemented in the all-electron DMol3 code [46,47] Double numerical plus polarization (DNP) basis set was used throughout the calculation. The convergence criteria were set to be $2 \times 10^{-5}$ Ha, 0.004 HaÅ$^{-1}$, and 0.005 Å for energy, force, and displacement convergence, respectively. A self-consistent field (SCF) density convergence with a threshold value of $1 \times 10^{-5}$ Ha was specified. $(2 \times 3)$ 29 Å thickness (7 CdS layers) surface unit cells have been used to represent the CdS {220} surface.

## 3. Results and discussion

Fig. 1a gives a schematic illustration for the formation of CdS@CDs/Pt-SAs. Briefly, ultrathin Cd(OH)$_2$@CDs nanosheets were firstly synthesized from the reaction of cadmium acetate with n-butylamine in a mixture of ethylene glycol and CDs aqueous solution by a solvent-thermal method (i). SEM image (Fig. 1b) of the obtained Cd(OH)$_2$@CDs precursor shows that it consists of large amount of nanosheets with average thickness of ˜7 nm, which is much thinner than the obtained Cd (OH)$_2$ nanoplates without CDs (Fig. S1a). TEM image as shown in Fig. 1c further reveals the Cd(OH)$_2$ ultrathin nanosheets features embedded many CDs with an average diameter of ˜4 nm (Fig. S1b). Then the as-synthesized Cd(OH)$_2$@CDs nanosheets were transformed into porous CdS@CDs nanosheets by sulfidation with Na$_2$S (ii). After converting to CdS@CDs, the surface becomes rough and maintains the original shape (Fig. S2a). Finally, the Pt single atoms were anchored onto the surfaces of CdS@CDs nanosheets by *in-situ* reduction of H$_2$PtCl$_6$ with CDs (iii). The HRSEM image (Fig. 1d) and the inset of HRTEM image in Fig. 1e confirm the porous structure of CdS@CDs/Pt-SAs nanosheets. The SAED pattern (the up-right inset in Fig. 1e) of the CdS@CDs/Pt-SAs reveals three diffraction rings corresponding to the (111), (220) and (311) planes of CdS, which is consistent with the XRD (Figure S3). The interplanar spacing of 0.34 nm, 0.21 nm and 0.18 nm over CdS@CDs/Pt-SAs nanosheets based on the HRTEM image (Fig. S2b) belong to the (111), (220) and (311) planes of cubic phase of CdS, respectively. The Pt signals cannot be detected here because of its atomic nature. Fig. 1e gives the HAADF-STEM image of CdS@CDs/Pt-SAs. It clearly shows that the bright spots corresponding to Pt atoms (marked with red circles) are uniformly dispersed on the CdS@CDs nanosheets. The EDS spectrum and elemental mapping demonstrate that Pt atoms are distributed evenly in the sample (Fig. 1f, g).

The local structure and coordination envrionment of the Pt single atoms are invetigaged by synchrotron-based X-ray absorption spectroscopy (XAS). Compared to the standard samples of PtO$_2$ and Pt foil, as revealed in Fig. 2a, the Pt L$_3$-edge X-ray absorption near-edge spectroscopy (XANES) of CdS@CDs/Pt-SAs demonstrates the existence of Pt-S bond, confirming that Pt exists exclusively as isolated single atoms. Fig. 2b gives the extended X-ray absorption fine structure spectroscopy (EXAFS) to probe the local structure environment of Pt atoms in CdS@CDs. EXAFS of CdS@CDs/Pt-SAs just gives one single sharp peak with total Gaussian distribution at about 2.3 Å, which is drastically different from the standard compound PtO$_2$ (gives an about 1.9 Å bond length) and Pt foil (contributions at a distance of ˜ 2.9 Å). The EXAFS part with the data-fitting in R space was carried out to determine the short-range local coordination structure including distances (R) and coordination number (CN) around the studied platinum atoms. On the basis of EXAFS fitting results (Fig. 2c and Table S1), a strong peak at ca. 2.3 Å with CN of *ca.* 4 was identified for the Pt-S shell, which is attributed by the scattering between platinum center and the sulfur atoms from the substrate. No significant other contributions such as ionic Pt-O and metallic Pt-Pt or Pt-Cd components have been observed. The results are consistent with the XPS analysis, confirming that the dispersed Pt atoms are stabilized through the Pt-S bond. Fig. 2d is the XPS spectra to

further prove the chemical composition and states of Cd, S and Pt in the sample. It is observed that binding energies of S 2p was at 161.4 and 162.45 eV in CdS@CDs nanosheets. Meanwhile, for CdS@CDs/Pt-SAs, the binding energies of S 2p was determined to be 161.25 and 162.2 eV [48]. The spectra can be convoluted into 3 peaks, where the signal at 162.7 eV can be attributed to the formation of Pt-S bond in CdS@CDs/Pt-SAs [40]. Moreover, the binding energies of Pt 4f in CdS@CDs/Pt-SAs (72.59 eV, 75.91 eV) are larger than those in CdS@CDs/Pt-NPs (72.43 eV, 75.75 eV) (Fig. S4a), indicating more metallic state Pt existed in the CdS@CDs/Pt-NPs [49–51]. In detail, the Pt 4f spectrum in CdS@CDs/Pt-SAs shown in Fig. S4b can be convoluted into 2 peaks corresponding to the Pt$^{\delta+}$ ($\delta$ = 0, 2). Furthermore, the binding energies of the Pt 4f$_{7/2}$ and 4f$_{5/2}$ shifted positively by ~1.0 eV, which is larger than that over Pt NPs in CdS@CDs/Pt-NPs (Fig. S4b, c). This phenomenon could be ascribed to the electronic interaction between Pt-SAs bonds with S, which was corroborated by the shift of S 2p peak to a lower binding energy (Fig. 2d) [52]. The peaks of Cd 3d$_{5/2}$ and Cd 3d$_{3/2}$ in the Cd 3d spectrum at 405.1 eV and 411.8 eV, respectively, are originating from Cd$^{2+}$ in CdS (Fig. S4d) [53]. Thus the coordination of sulfur with Pt-SAs slightly reduced the binding energy of Cd 3d, indicating the presence of Pt-SAs increased the electron density. Fig. 2e gives the time-resolved transient PL decay spectra of CdS@CDs/Pt-SAs exhibits more rapid decay than that of CdS@CDs, revealing that platinum component produces better trapping ability (Table S2). And the lowest PL intensity (Fig. 2f) and the lowest of decay life time of CdS@CDs/Pt-SAs compared to samples of CdS@CDs/Pt-NPs and CdS@CDs also implies its low recombination rate, good electron-hole separation capacity, and long-survived photogenerated electrons. The CdS@CDs nanosheets can absorb visible light with an absorption edge of about 613 nm, which corresponds to a bandgap of 2.02 eV. The addition of Pt single atoms result in a little blue shift of the absorption edge (Fig. S5a, b). The quantum efficiency (QE) of photocatalytic hydrogen production over CdS@CDs/Pt-SAs photocatalyst as a function of the wavelength of incident light was tested. Notably, as shown in Fig. S5c, the overall trend of QE is related to the absorbance of the catalyst. The QE is ˜29.8% at 400 nm when used 10 mg of the catalyst in the system.

Additionally, the charge carrier separation capability in CdS@CDs/Pt-SAs was also demonstrated by photocurrent production in photoelectrochemical tests. The CdS@CDs/Pt-SAs sample shows the highest photocurrent response (Fig. S6a), implying its high capacity in producing high density of photo-generated electrons. Fig. S6b shows the photo-induced EIS for CdS@CDs, CdS@CDs/Pt-NPs, and CdS@CDs/Pt-SAs. CdS@CDs/Pt-SAs exhibits a much lower charge-transfer resistance than CdS@CDs and CdS@CDs/Pt- NPs. The results are consistent with the conclusion of PL emission (Fig. 2f), testifying the CdS@CDs/Pt-SAs can provide an effective transport pathways to enhance harvest of incident light by multiple scattering within the porous nanosheets, and thus promote photocatalytic hydrogen production.

Theoretically, the role of Pt single atoms on the CdS nanosheets is also disussed. CdS {220} and single CdS/Pt-SAs {220} structure have been optimized using GGA-PBE [54]. Mulliken population analysis and density of states over these two structure were calculated. As shown in Fig. 3, the computational results indicate that with the introduction of Pt single atoms onto the CdS surface, new empty bands produced near the Fermi level. Population analysis shows that there are 8.9 electrons in the d-band of single Pt atom in the CdS/Pt-SAs, thus the d-band occupancy is not affected during the bonding of Pt and CdS, and the empty orbitals still exist. These empty bands are closer to the Fermi level than pure CdS, which will facilitate the accommodation of photogenerated electrons generated in the photo-induced process. Because of the high atomic utilization of monoatomic dispersed materials with maximize active sites, a large number of empty bands accommodate photogenerated electrons on the surface of the single CdS/Pt-SAs are expected, and thus leads to the reduction of water for highly efficient hydrogen evolution.
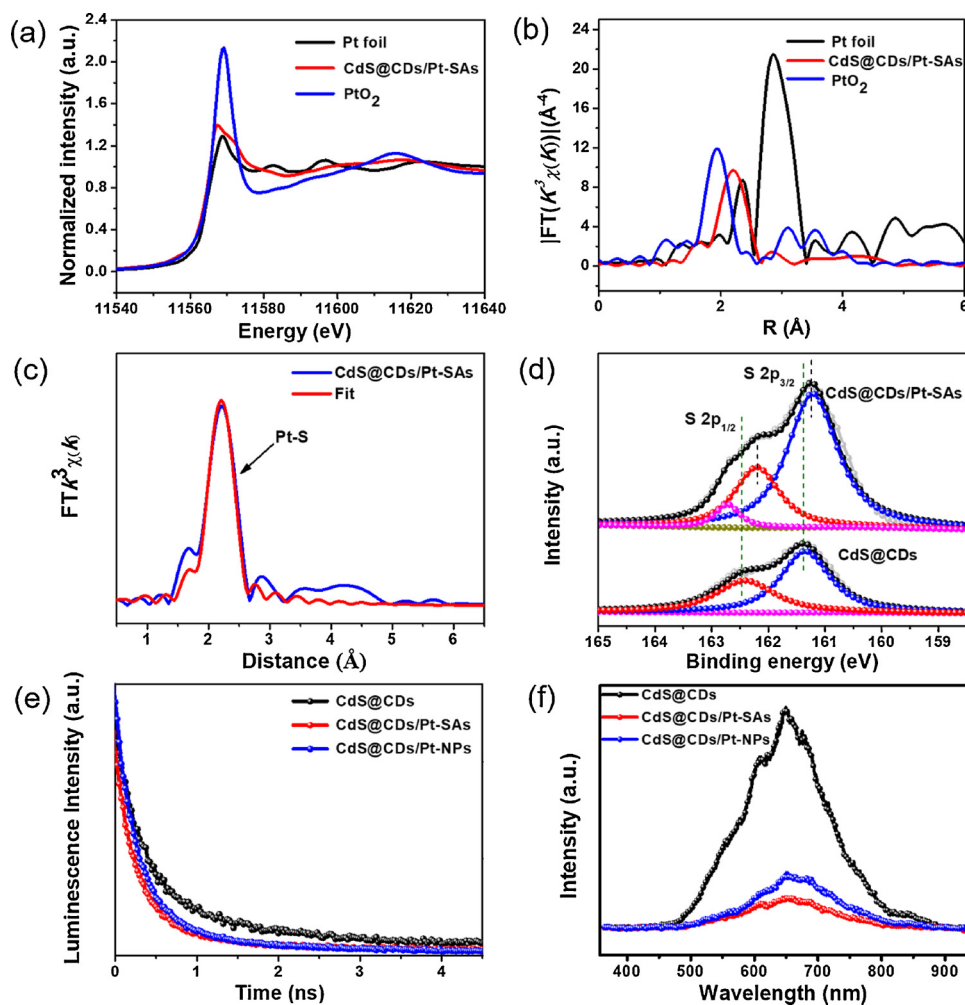
**Fig. 2.** (a) The normalized Pt-edge XANES spectra of different samples and references. (b) Fourier transform magnitudes of the experimental Pt L3-edge EXAFS spectra of Pt foil, PtO$_2$, and CdS@CDs/Pt-SAs. (c) Fourier-transformed magnitudes of Pt L3-edge EXAFS spectra in R space for CdS@CDs/Pt-SAs. (d) The XPS spectra of S 2p for CdS@CDs and CdS@CDs/Pt-SAs. (e) Time-resolved transient PL decay spectra and (f) PL spectra of CdS@CDs, CdS@CDs/Pt-NPs and CdS@CDs/Pt-SAs.

Fig. 4a compares the photocatalytic H$_2$ evolution performance of single CdS, CdS/Pt-NPs, CdS@CDs, CdS@CDs/Pt-SAs (1.15 wt% Pt), and CdS@CDs/Pt-NPs (1.54 wt% Pt). The result shows that CdS@CDs gives the lowest activity with H$_2$ evolution rate of 0.344 mmol h$^{-1}$ g$^{-1}$. Meanwhile, the H$_2$ evolution rate over CdS without CDs is slightly higher than CdS@CDs. UV-*vis* absorption spectra (Fig. S5a) show that although the addition of the CDs improves the visible light absorption, the bandgap of CdS@CDs nanosheets is slightly decreased in comparison with single CdS, reducing the reduction ability of photogenic electrons, even Pt NPs were introduced onto the CdS@CDs surface.
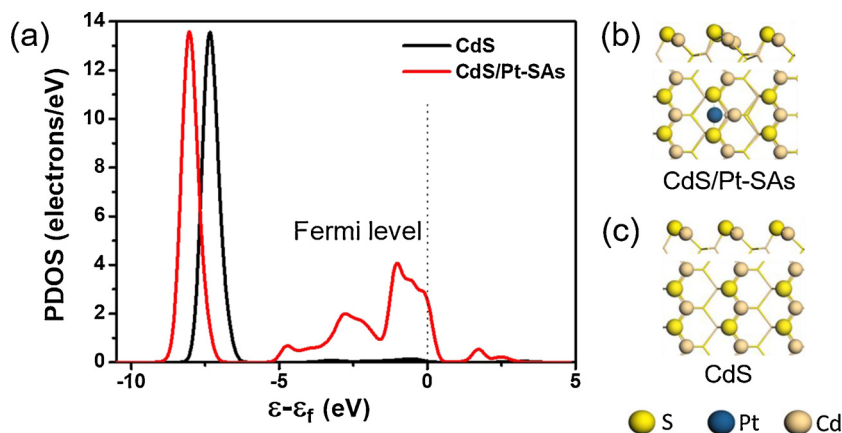


**Fig. 3.** Partial density of states (PDOS, d band) and optimized structure of CdS/Pt-SAs {220} and CdS {220}. (a) d-PDOS of CdS/Pt-SAs {220} and CdS {220}, (b) optimized CdS/Pt-SAs {220}, and (c) CdS {220} structure (Top and side view).
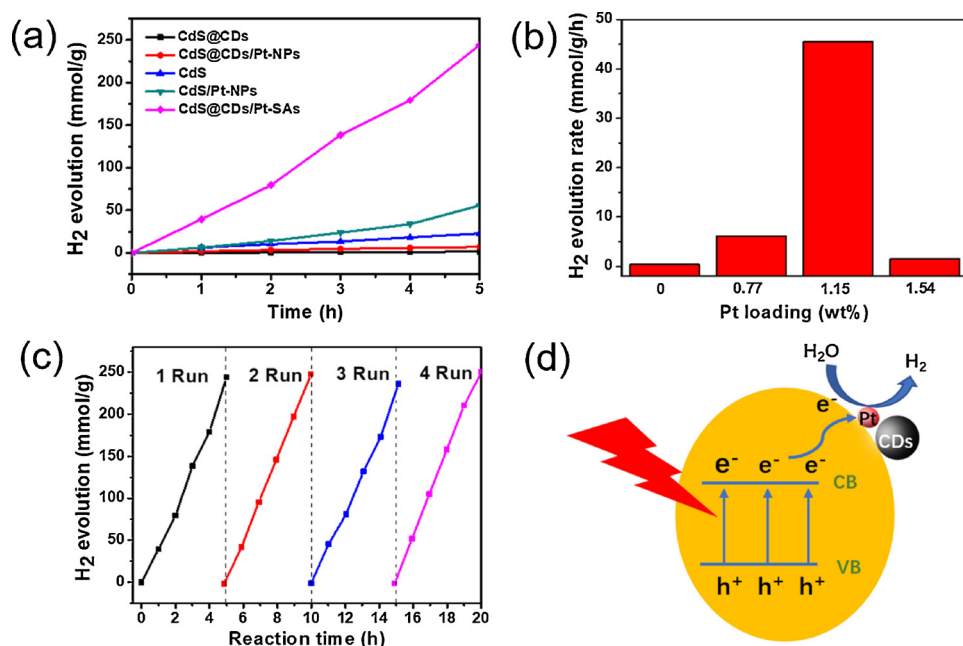
**Fig. 4.** (a) Photocatalytic H$_2$ evolution over CdS@CDs, CdS@CDs/Pt-NPs, CdS, CdS/Pt-NPs, and CdS@CDs/Pt-SAs under simulated sunlight irradiation. (b) Pt loading effects on the photocatalytic activities of CdS@CDs for H$_2$ production. (c) Photocatalyst lifespan tests over CdS@CDs/Pt-SAs. (d) Schematic illustration of the hydrogen evolution mechanism.

However, when single-atom Pt introduced as cocatalysts, the CdS@CDs/Pt-SAs shows a significant enhancement towards H$_2$ generation with a rate of 45.5 mmol h$^{-1}$ g$^{-1}$ under simulated sunlight irradiation, which is as nearly 133 folds as that of CdS@CDs. And it also displays much higher performance than CdS@CDs/Pt-NPs, CdS/Pt-NPs and CdS. Moreover, the stable H$_2$ evolution rate of CdS@CDs/Pt-SAs reflects the stability of single-atom Pt in the CdS@CDs. Compared to the reported noble-metal photocataysts (Table S3), the CdS@CDs/Pt-SAs exhibited the highest activity. Fig. 4b exhibits different activities with the Pt loadings varied from 0.77 wt% to 1.54 wt% associated with an average H$_2$ generation rate ranging from 6.12 to 1.45 mmol h$^{-1}$ g$^{-1}$. It is noted that if the Pt loading is 0.77 wt%, the hydrogen evolution rate (6.12 mmol h$^{-1}$ g$^{-1}$) has an obvious drop compared to that loading 1.15 wt% Pt, which could be attributed to the decreased Pt atoms density with low quantity of active sites. While further increased Pt loading to1.54 wt% resulted in the formation of Pt NPs (Fig. S7a), the activity of which was also decreased. The results indicated that a certain single atom density is essential to reach optimal catalytic activity. When the single CdS nanosheets synthesized without CDs loaded 1.15 wt% Pt species, Pt nanoparticles are formed on the surfaces of CdS (Fig. S7b), proving that reduction effectiveness of CDs on the achievement of Pt single atoms. Furthermore, the CdS@CDs/Pt-SAs can be experienced 20 h without losing activity (Fig. 4c). The analyses of XPS, HAADF-STEM image, and EDS mapping of CdS@CDs/Pt-SAs after the tests (Fig. S8 and Fig. S9) show that no significant changes occur, showing its good stability. More importantly, Pt single atoms have the most significant impact in improving charge separation over CdS nanosheets, accelerating the electron transfer to avoid recombination of photo-induced electron-hole pairs, and simultaneously accept electrons as active sites for the reduction of water under light irradiation (Fig. 4d).

## 4. Conclusion

In summary, we have developed a simple and reproducible route to synthesize highly efficient solar-driven CdS@CDs/Pt-SAs nanophotocatalysts with the *in-situ* reduction of metal precursor by CDs. The HAADF-STEM and the Pt-edge XANES spectra of catalyst confirmed the dominant presence of isolated Pt atoms without Pt nanoparticles formation. It was very interesting that the as-achieved CdS@CDs/Pt-SAs (1.15 wt% Pt loading) catalyst has remarkably higher catalytic activity

than CdS@CDs/Pt-NPs and bare CdS in the solar-driven hydrogen production. It shows a H$_2$ generation rate of 45.5 mmol h$^{-1}$ g$^{-1}$, which is as nearly 133 folds as that of CdS@CDs. The formed Pt-S bond makes Pt single-atoms very stable, rendering it to be reused for 20 h without losing activity. The present work opens a new way to prepare many types of metal single atoms assisted photocalysts, electrocatalysts and other catalysts to drive various organic synthesis with enhanced performance.

## Declaration of Competing Interest

The authors declare no competing financial interest.

## Appendix A. Supplementary data

Supplementary material related to this article can be found, in the online version, at doi:https://doi.org/10.1016/j.apcatb.2019.118036.

## References

[1] L. Liao, Q. Zhang, Z. Su, Z. Zhao, Y. Wang, Y. Li, X. Lu, D. Wei, G. Feng, Q. Yu, X. Cai, J. Zhao, Z. Ren, H. Fang, F. Robles-Hernandez, S. Baldelli, J. Bao, Efficient solar water-splitting using a nanocrystalline CoO photocatalyst, Nat. Nanotechnol. 9 (2014) 69–73 https://www.nature.com/articles/nnano.2013.272.

[2] D.J. Martin, P.J. Reardon, S.J.A. Moniz, J. Tang, Visible light-driven pure water splitting by a nature-inspired organic semiconductor-based system, J. Am. Chem. Soc. 136 (2014) 12568–12571, https://doi.org/10.1021/ja506386e.

[3] X. Wang, S. Blechert, M. Antonietti, Polymeric graphitic carbon nitride for heterogeneous photocatalysis, ACS Catal. 2 (2012) 1596–1606, https://doi.org/10.1021/cs300240x.

[4] L. Weng, H. Zhang, A.O. Govorov, M. Ouyang, Hierarchical synthesis of non-centrosymmetric hybrid nanostructures and enabled plasmon-driven photocatalysis, Nat. Commun. 5 (2014) 4792 https://www.nature.com/articles/ncomms5792.

[5] Z. Tan, L. Ouyang, J. Liu, H. Wang, H. Shao, M. Zhu, Hydrogen generation by hydrolysis of Mg-Mg$_2$Si composite and enhanced kinetics performance from introducing of MgCl$_2$ and Si, Int. J. Hydrogen Energy 43 (2018) 2903–2912, https://

doi.org/10.1016/j.ijhydene.2017.12.163.

[6] M. Huang, L. Ouyang, Z. Chen, C. Peng, X. Zhu, M. Zhu, Hydrogen production via hydrolysis of Mg-oxide composites, Int. J. Hydrogen Energy 42 (2017) 22305–22311, https://doi.org/10.1016/j.ijhydene.2016.12.099.

[7] L. Ouyang, X. Yang, M. Zhu, J. Liu, H. Dong, D. Sun, J. Zou, X. Yao, Enhanced hydrogen storage kinetics and stability by synergistic effects of in situ formed CeH$_{2.73}$ and Ni in CeH$_{2.73}$-MgH$_2$-Ni nanocomposites, J. Phys. Chem. C 118 (2014) 7808–7820, https://doi.org/10.1021/jp500439n.

[8] M. Zhu, H. Wang, L. Ouyang, M. Zeng, Composite structure and hydrogen storage properties in Mg-base alloys, Int. J. Hydrogen Energy 31 (2006) 251–257, https://doi.org/10.1016/j.ijhydene.2005.04.030.

[9] H. Zhong, L. Ouyang, M. Zeng, J. Liu, H. Wang, H. Shao, Michael Felderhoff, M. Zhu, Realizing facile regeneration of spent NaBH$_4$ with Mg–Al alloy, J. Mater. Chem. A 7 (2019) 10723–10728, https://doi.org/10.1039/C9TA00769E.

[10] D.W. Wakerley, M.F. Kuehnel, K.L. Orchard, K.H. Ly, T.E. Rosser, E. Reisner, Solar-driven reforming of lignocellulose to H$_2$ with a CdS/CdOx photocatalyst, Nat. Energy 2 (2017) 17021 https://www.nature.com/articles/nenergy201721.

[11] M. Liu, Y. Chen, J. Su, J. Shi, X. Wang, L. Guo, Photocatalytic hydrogen production using twinned nanocrystals and an unanchored NiS$_x$ co-catalyst, Nat. Energy 1 (2016) 16151 https://www.nature.com/articles/nenergy2016151.

[12] K. Maeda, G. Sahara, M. Eguchi, O. Ishitani, Hybrids of a ruthenium(II) polypyridyl complex and a metal oxide nanosheet for dye-sensitized hydrogen evolution with visible light: effects of the energy structure on photocatalytic activity, ACS Catal. 5 (2015) 1700–1707, https://doi.org/10.1021/acscatal.5b00040.

[13] S. Guan, X. Fu, Y. Zhang, Z. Peng, B- NiS modified CdS nanowires for photocatalytic H$_2$ evolution with exceptionally high efficiency, Chem. Sci. 9 (2018) 1574–1585, https://doi.org/10.1039/C7SC03928J.

[14] Y. Hu, X. Gao, L. Yu, Y. Wang, J. Ning, S. Xu, X. Lou, Carbon-coated CdS petalous nanostructures with enhanced photostability and photocatalytic activity, Angew. Chem. Int. Ed. 52 (2013) 5636–5639, https://doi.org/10.1002/anie.201301709.

[15] Q. Lia, T. Shi, X. Li, K. Lva, M. Lia, F. Liu, H. Li, M. Lei, Remarkable positive effect of Cd(OH)$_2$ on CdS semiconductor for visible-light photocatalytic H$_2$ production, Appl. Catal. B 229 (2018) 8–14, https://doi.org/10.1016/j.apcatb.2018.01.078.

[16] C. Bie, J. Fu, B. Cheng, L. Zhang, Ultrathin CdS nanosheets with tunable thickness and efficient photocatalytic hydrogen generation, Appl. Surf. Sci. 462 (2018) 606–614, https://doi.org/10.1016/j.apsusc.2018.08.130.

[17] X.-J. Wu, J. Chen, C. Tan, Y. Zhu, Y. Han, H. Zhang, Controlled growth of high-density CdS and CdSe nanorod arrays on selective facets of two-dimensional semiconductor nanoplates, Nat. Chem. 8 (2016) 470–475 https://www.nature.com/articles/nchem.2473.

[18] X. Huang, B. Zheng, Z. Liu, C. Tan, J. Liu, B. Chen, H. Li, J. Chen, X. Zhang, Z. Fan, W. Zhang, Z. Guo, F. Huo, Y. Yang, L.-H. Xie, W. Huang, H. Zhang, Coating two-dimensional nanomaterials with metal-organic frameworks, ACS Nano 8 (2014) 8695–8701, https://doi.org/10.1021/nn503834u.

[19] X. Wang, K. Maeda, X. Chen, K. Takanabe, K. Domen, Y. Hou, X. Fu, M. Antonietti, Hydrogen evolution by mesoporous graphitic carbon nitride with visible light, J. Am. Chem. Soc. 131 (2009) 1680–1681, https://doi.org/10.1021/ja809307s.

[20] C. Lin, L. Yang, L. Ouyang, J. Liu, H. Wang, M. Zhu, A new method for few-layer graphene preparation via plasma-assisted ball milling, J. Alloys. Compd. 728 (2017) 578–584, https://doi.org/10.1016/j.jallcom.2017.09.056.

[21] L. Ouyang, Z. Cao, H. Wang, R. Hu, M. Zhu, Application of dielectric barrier discharge plasma-assisted milling in energy storage materials – a review, J. Alloys. Compd. 691 (2017) 422–435, https://doi.org/10.1016/j.jallcom.2016.08.179.

[22] C. Zhu, C. Liu, Y. Fu, J. Gao, H. Huang, Y. Liu, Z. Kang, Construction of CdS/CdS photocatalysts for stable and efficient hydrogen production in water and seawater, Appl. Catal. B 242 (2019) 178–185, https://doi.org/10.1016/j.apcatb.2018.09.096.

[23] Q. Li, B. Guo, J. Yu, J. Ran, B. Zhang, H. Yan, J. Gong, Highly efficient visible-light-driven photocatalytic hydrogen production of CdS-cluster-decorated graphene nanosheets, J. Am. Chem. Soc. 133 (2011) 10878–10884, https://doi.org/10.1021/ja2025454.

[24] Q. Xiang, J. Yu, M. Jaroniec, Synergetic effect of MoS$_2$ and graphene as cocatalysts for enhanced photocatalytic H$_2$ production activity of TiO$_2$ nanoparticles, J. Am. Chem. Soc. 134 (2012) 6575–6578, https://doi.org/10.1021/ja302846n.

[25] M. Luo, W. Yao, C. Huang, Q. Wu, Q. Xu, Shape effects of Pt nanoparticles on hydrogen production via Pt/CdS photocatalysts under visible light, J. Mater. Chem. A 3 (2015) 13884–13891, https://doi.org/10.1039/C5TA00218D.

[26] J. Fanga, W. Wang, C. Zhu, L. Fang, J. Jin, Y. Ni, C. Lua, Z. Xu, CdS/Pt photocatalytic activity boosted by high-energetic photons based on efficient triplet–triplet annihilation upconversion, Appl. Catal. B 217 (2017) 100–107, https://doi.org/10.1016/j.apcatb.2017.05.069.

[27] F. Chen, X. Jiang, L. Zhang, R. Lang, B. Qiao, Single-atom catalysis: bridging the homo-and heterogeneous catalysis, Chin. J. Catal. 39 (2018) 893–898, https://doi.org/10.1016/S1872-2067(18)63047-5.

[28] G. Gao, Y. Jiao, E.R. Waclawik, A. Du, Single atom (Pd/Pt) supported on graphitic carbon nitride as an efficient photocatalyst for visible-light reduction of carbon dioxide, J. Am. Chem. Soc. 138 (2016) 6292–6297, https://doi.org/10.1021/jacs.6b02692.

[29] Y. Sui, S. Liu, T. Li, Q. Liu, T. Jiang, Y. Guo, J.-L. Luo, Atomically dispersed Pt on specific TiO$_2$ facets for photocatalytic H$_2$ evolution, J. Catal. 353 (2017) 250–255, https://doi.org/10.1016/j.jcat.2017.07.024.

[30] N. Cheng, S. Stambula, D. Wang, M.N. Banis, J. Liu, A. Riese, B. Xiao, R. Li, T.-K. Sham, L.-M. Liu, G.A. Botton, X. Sun, Platinum single-atom and cluster catalysis of the hydrogen evolution reaction, Nat. Commun. 7 (2016) 13638 https://www.nature.com/articles/ncomms13638.

[31] G. Han, Y. Jin, R.A. Burgess, N.E. Dickenson, X. Cao, Y. Sun, Visible-light-driven valorization of biomass intermediates integrated with H$_2$ production catalyzed by ultrathin Ni/CdS nanosheets, J. Am. Chem. Soc. 139 (2017) 15584–15587, https://doi.org/10.1021/jacs.7b08657.

[32] E.C. Tyo, S. Vajda, Catalysis by clusters with precise numbers of atoms, Nat. Nanotechnol. 10 (2015) 577–588 https://www.nature.com/articles/nnano.2015.140.

[33] T. Simon, N. Bouchonville, M.J. Berr, A. Vaneski, A. Adrovic, D. Volbers, R. Wyrwich, M. Doblinger, A.S. Susha, A.L. Rogach, F. Jackel, J.K. Stolarczyk, J. Feldmann, Redox shuttle mechanism enhances photocatalytic H$_2$ generation on Ni-decorated CdS nanorods, Nat. Mater. 13 (2014) 1013–1018 https://www.nature.com/articles/nmat4049.

[34] C. Wang, Q. Chen, Reduction-induced decomposition: spontaneous formation of monolithic nanoporous metals of tunable structural hierarchy and porosity, Chem. Mater. 30 (2018) 3894–3900, https://doi.org/10.1021/acs.chemmater.8b01431.

[35] L. Ma, K. Chen, F. Nan, J.-H. Wang, D.-J. Yang, L. Zhou, Q.-Q. Wang, Improved hydrogen production of Au-Pt-CdS hetero-nanostructures by efficient plasmon-induced multipathway electron transfer, Adv. Funct. Mater. 26 (2016) 6076–6083, https://doi.org/10.1002/adfm.201601651.

[36] I. Vamvasakis, B. Liu, G.S. Armatas, Size effects of platinum nanoparticles in the photocatalytic hydrogen production over 3D mesoporous networks of CdS and Pt nanojunctions, Adv. Funct. Mater. 26 (2016) 8062–8071, https://doi.org/10.1002/adfm.201603292.

[37] G. Zhao, Y. Sun, W. Zhou, X. Wang, K. Chang, G. Liu, H. Liu, T. Kako, J. Ye, Superior photocatalytic H$_2$ production with cocatalytic Co/Ni species anchored on sulfide semiconductor, Adv. Mater. 29 (2017) 1703258, , https://doi.org/10.1002/adma.201703258.

[38] X. Fang, Q. Shang, Y. Wang, L. Jiao, T. Yao, Y. Li, Q. Zhang, Y. Luo, H. Jiang, Single Pt atoms confined into a metal-organic framework for efficient photocatalysis, Adv. Mater. 30 (2018) 1705112, , https://doi.org/10.1002/adma.201705112.

[39] Y. Xue, B. Huang, Y. Yi, Y. Guo, Z. Zuo, Y. Li, Z. Jia, H. Liu, Y. Li, Anchoring zero valence single atoms of nickel and iron on graphdiyne for hydrogen evolution, Nat. Commun. 9 (2018) 1460 https://www.nature.com/articles/s41467-018-03896-4.

[40] X. Li, W. Bi, L. Zhang, S. Tao, W. Chu, Q. Zhang, Y. Luo, C. Wu, Y. Xie, Single-atom Pt as co-catalyst for enhanced photocatalytic H$_2$ evolution, Adv. Mater. 28 (2016) 2427–2431, https://doi.org/10.1002/adma.201505281.

[41] Q. Zhao, J. Sun, S. Li, C. Huang, W. Yao, W. Chen, T. Zeng, Q. Wu, Q. Xu, Single nickel atoms anchored on nitrogen-doped graphene as a highly active cocatalyst for photocatalytic H$_2$ evolution, ACS Catal. 8 (2018) 11863–11874, https://doi.org/10.1021/acscatal.8b03737.

[42] X. Wu, H. Zhang, J. Dong, M. Qiu, J. Kong, Y. Zhang, Y. Li, G. Xu, J. Zhang, J. Ye, Surface step decoration of isolated atom as electron pumping: atomic-level insights into visible-light hydrogen evolution, Nano Energy 45 (2018) 109–117, https://doi.org/10.1016/j.nanoen.2017.12.039.

[43] C. Gao, S. Chen, Y. Wang, J. Wang, X. Zheng, J. Zhu, L. Song, W. Zhang, Y. Xiong, Heterogeneous single-atom catalyst for visible-light-driven high-turnover CO$_2$ reduction: the role of electron transfer, Adv. Mater. 30 (2018) 1704624, , https://doi.org/10.1002/adma.201704624.

[44] G. Wei, K. Du, X. Zhao, Z. Wang, M. Liu, C. Li, H. Wang, C. An, W. Xing, Carbon quantum dot-induced self-assembly of ultrathin Ni(OH)$_2$ nanosheets: a facile method for fabricating three-dimensional porous hierarchical composite micro-nanostructures with excellent supercapacitor performance, Nano Res. 10 (2017) 3005–3017, https://doi.org/10.1007/s12274-017-1516-4.

[45] A.I. Frenkel, Q. Wang, N. Marinkovic, J.G. Chen, L. Barrio, R. Si, A.L. Camara, A.M. Estrella, J.A. Rodriguez, J.C. Hanson, Combining X-ray absorption and X-ray diffraction techniques for in situ studies of chemical transformations in heterogeneous catalysis: advantages and limitations, J. Phys. Chem. C 115 (2011) 17884–17890, https://doi.org/10.1021/jp205204e.

[46] B. Delley, An all-electron numerical method for solving the local density functional for polyatomic molecules, J. Chem. Phys. 92 (1990) 508–517, https://doi.org/10.1063/1.458452.

[47] B. Delley, From molecules to solids with the DMol$^3$ approach, J. Chem. Phys. 113 (2000) 7756–7764, https://doi.org/10.1063/1.1316015.

[48] L. Zhang, X. Fu, S. Meng, X. Jiang, J. Wang, S. Chen, Ultra-low content of Pt modified CdS nanorods: one-pot synthesis and high photocatalytic activity for H$_2$ production under visible light, J. Mater. Chem. A 3 (2015) 23732–23742, https://doi.org/10.1039/C5TA07459B.

[49] Z. Tian, S. Jiang, S. Liang, P. Shen, Synthesis and characterization of platinum catalysts on multiwalled carbon nanotubes by intermittent microwave irradiation for fuel cell applications, J. Phys. Chem. B 110 (2006) 5343–5350, https://doi.org/10.1021/jp056401o.

[50] F. Sen, G. Gokagac, Different sized platinum nanoparticles supported on carbon: an XPS study on these methanol oxidation catalysts, J. Phys. Chem. C 111 (2007) 5715–5720, https://doi.org/10.1021/jp068381b.

[51] C. Wang, H. Fan, X. Ren, Y. Wen, W. Wang, Highly dispersed PtO nanodots as efficient co-catalyst for photocatalytic hydrogen evolution, Appl. Surf. Sci. 462 (2018) 423–431, https://doi.org/10.1016/j.apsusc.2018.08.126.

[52] L. Guo, W. Jiang, Y. Zhang, J. Hu, Z. Wei, L. Wan, Embedding Pt nanocrystals in N-doped porous carbon/carbon nanotubes toward highly stable electrocatalysts for the oxygen reduction reaction, ACS Catal. 5 (2015) 2903–2909, https://doi.org/10.1021/acscatal.5b00117.

[53] X. Zong, H. Yan, G. Wu, G. Ma, F. Wen, L. Wang, C. Li, Enhancement of photocatalytic H$_2$ evolution on CdS by loading MoS$_2$ as cocatalyst under visible light irradiation, J. Am. Chem. Soc. 130 (2008) 7176–7177, https://doi.org/10.1021/ja8007825.

[54] J.P. Perdew, K. Burke, M. Ernzerhof, Generalized gradient approximation made simple, Phys. Rev. Lett. 77 (1996) 3865–3868, https://doi.org/10.1103/PhysRevLett.77.3865.